Structured Input-Output Tools for Modal Analysis of a Transitional Channel Flow

Talha Mushtaq*
University of Minnesota, Minneapolis, MN 55455, USA

Diganta Bhattacharjee†
University of Minnesota, Minneapolis, MN 55455, USA

Peter Seiler‡
University of Michigan, Ann Arbor, MI 48109, USA

Maziar S. Hemati§
University of Minnesota, Minneapolis, MN 55455, USA

Structured input-output (I/O) analysis has recently been proposed as a useful low-complexity technique for performing stability analysis of incompressible flows. In this paper, we show how structured I/O methods can be used for a modal analysis of a given incompressible fluid model. We exploit the fact that the same convective nonlinearity acts on the evolution of every state to impose additional structure on the I/O analysis and consequently, uncover the underlying physical mechanisms from I/O mode shapes, frequency modes and I/O gain computations. This additional structure results in lower estimates for the I/O gain upper bound compared to the traditional analysis, thus indicating a larger margin to instability. Additionally, we propose a power-iteration technique that imposes the repeating structure of the nonlinearity to not only compute the lower bounds on the I/O gain but also extract the optimal forcing and response modes that are consistent with the structure of the nonlinear flow physics. The approach is demonstrated on an incompressible channel flow at $Re = 690$.

I. Introduction

Input-output (I/O) and resolvent analysis methods have proven to be valuable tools for elucidating structure and physics in many complex flows [1]. These methods are physics-based and complement prevailing data-driven modal analysis methods that have been adopted in a variety of studies [2–4]. I/O methods decompose the governing Navier-Stokes equations (NSE) into a feedback interconnection between linear dynamics and the relevant nonlinear terms. Traditional I/O analysis proceeds to treat forcing from the nonlinear terms on the linear dynamics as an implicit (unstructured) forcing. In so doing, efficient tools from linear systems theory can be applied to identify coherent structures associated with amplification mechanisms in the flow. Optimal input (forcing) and output (response) modes associated with the linear dynamics have been shown to highlight known amplification mechanisms in the fluid dynamics—e.g., lift-up mechanisms in transitional wall-bounded shear flows. Despite the successes of linear analysis techniques, it is well-established that consideration for nonlinear flow interactions is necessary for addressing questions associated with the nonlinear flow physics. Unfortunately, currently available nonlinear analysis tools tend to suffer from substantial challenges with computational complexity, which has limited adoption of these powerful analysis tools [5–9].

Recently, structured I/O methods have been proposed as a computationally tractable approach to account for the structure of the nonlinear forcing within the linear analysis framework [10]. The structured I/O approach proposed in [10] applies the structured singular value (SSV) analysis methods of robust control theory [11, 12] to the incompressible Navier-Stokes equations. The authors showed that imposing physical structure on the nonlinear forcing within the I/O analysis results in a broader range of amplification mechanisms than linear I/O methods. However, these mechanisms had to be inferred through a careful analysis of the structured I/O gains themselves, and not from an analysis of associated

---

*Graduate Research Assistant, Aerospace Engineering and Mechanics.
†Postdoctoral Research Associate, Aerospace Engineering and Mechanics, AIAA Member.
‡Associate Professor, Electrical Engineering and Computer Science, AIAA Associate Fellow.
§Associate Professor, Aerospace Engineering and Mechanics, AIAA Associate Fellow

mode shapes; an ability to extract forcing and response mode shapes from the structured I/O analysis would have further informed understanding and interpretation of the underlying physics.

In this paper, we show that computations of the SSV upper and lower bound can be used to extract optimal *I/O gains*, and forcing and response *mode shapes* within the structured I/O framework. The ability to extract mode shapes in addition to optimal I/O gains creates opportunities to probe the structure of the underlying physics and extract more insight about the fluid dynamics. Additionally, we impose additional structure on the nonlinear signals for both upper- and lower bound calculations, taking advantage of the fact that the convective nonlinearity in the incompressible NSE is repeated. As shown in [13], accounting for this additional repeated structure of the nonlinearity can reduce conservatism in the gain computations and refine the structured I/O analysis even further. Additionally, we show that when the gap between the upper and lower bound is sufficiently tight (say 1%), then appropriate application of the singular value decomposition (SVD) to the upper-bound calculation can be used to obtain the I/O mode shapes. We use the channel flow system as an example case to demonstrate the various features of the structured I/O analysis framework, including gain computations, mode shape extraction, temporal frequency analysis, and SSV bound quality analysis.

The paper is organized as follows. Section II discusses the input-output analysis framework, which is followed by discussion of the methods for computing the mode shapes and the SSV bounds in Section III. Section IV contains the results for the channel flow system and a brief discussion about the interpretation of the mode shapes.

II. Navier-Stokes Equations: An Input-Output Model

In this section, we will briefly describe the steps required to establish a structured I/O model of the incompressible NSE. The structured I/O approach yields a reduced-complexity framework that approximates the convective nonlinearity in the incompressible NSE as a repeated feedback forcing. Thus, we use the structured I/O method to compute the worst-case amplifications (I/O gains) and highlight the destabilizing flow mechanisms (mode shapes) that are consistent with the underlying flow physics. Certainly, the structured I/O analysis is not a replacement for high-fidelity direct numerical simulations (DNS) but an aid for the user to extract mechanisms from the governing equations themselves in a simulation-free manner. DNS generates heaps of data, but physical insights and mechanisms are not delivered directly. Instead, data-driven modal analysis methods are used to provide a way for analyzing that data. Furthermore, I/O methods help improve the estimates of desirable parameters and initial conditions for DNS runs, which circumvents the issue of performing a series of numerical simulations to search for these parameters. Next, we will derive the structured I/O model of the NSE.

A. Structured Input-Output Model

We start with the non-dimensionalized perturbation equations associated with the incompressible NSE:

$$\partial_t \mathbf{u} = \frac{1}{Re}\nabla^2 \mathbf{u} - \nabla p - \mathbf{u} \cdot \nabla \mathbf{U}_b - \mathbf{U}_b \cdot \nabla \mathbf{u} - \mathbf{u} \cdot \nabla \mathbf{u}$$
$$\nabla \cdot \mathbf{u} = 0 \tag{1}$$

where $\mathbf{u} = \begin{bmatrix} u & v & w \end{bmatrix}^{\mathrm{T}}$ and $\mathbf{U}_b = \begin{bmatrix} U & V & W \end{bmatrix}^{\mathrm{T}}$ are the perturbation and baseflow velocity vectors, p is the perturbation pressure, Re is the Reynolds number, $\nabla = \begin{bmatrix} \partial_x & \partial_y & \partial_z \end{bmatrix}^{\mathrm{T}}$ is the gradient operator and $\nabla^2 = \partial_x^2 + \partial_y^2 + \partial_z^2$ is the Laplacian. We partition NSE into a linear part denoted as $\mathcal{L}(\mathbf{u}, p) = \frac{1}{Re}\nabla^2 \mathbf{u} - \nabla p - \mathbf{U}_b \cdot \nabla \mathbf{u} - \mathbf{u} \cdot \nabla \mathbf{U}_b$ and the associated nonlinear convective part $\mathbf{f} = -\mathbf{u} \cdot \nabla \mathbf{u}$. As noted by the authors in [10], the nonlinear forcing term $\mathbf{f}$ can be written as a matrix-vector product:

$$\mathbf{f} = \begin{bmatrix} -\mathbf{u}^{\mathrm{T}} & 0 & 0 \\ 0 & -\mathbf{u}^{\mathrm{T}} & 0 \\ 0 & 0 & -\mathbf{u}^{\mathrm{T}} \end{bmatrix} \begin{bmatrix} \nabla u \\ \nabla v \\ \nabla w \end{bmatrix} = \begin{bmatrix} -\mathbf{u}^{\mathrm{T}} & 0 & 0 \\ 0 & -\mathbf{u}^{\mathrm{T}} & 0 \\ 0 & 0 & -\mathbf{u}^{\mathrm{T}} \end{bmatrix} \begin{bmatrix} \nabla & 0 & 0 \\ 0 & \nabla & 0 \\ 0 & 0 & \nabla \end{bmatrix} \begin{bmatrix} u \\ v \\ w \end{bmatrix} = \mathbf{u}_\gamma \mathbf{y} \tag{2}$$

where $\mathbf{u}_\gamma = \mathrm{diag}(-\mathbf{u}^{\mathrm{T}}, -\mathbf{u}^{\mathrm{T}}, -\mathbf{u}^{\mathrm{T}})$ is the velocity matrix and $\mathbf{y} = \mathrm{diag}(\nabla, \nabla, \nabla)\mathbf{u}$ are the velocity gradients. Here, $\mathrm{diag}(\cdot)$ represents a block-diagonal matrix. Thus, we have the following dynamical system:

$$\begin{aligned} \partial_t \mathbf{u} &= \mathcal{L}(\mathbf{u}, p) + \mathbf{f}, \\ \nabla \cdot \mathbf{u} &= 0, \\ \mathbf{y} &= \mathrm{diag}(\nabla, \nabla, \nabla)\mathbf{u}. \end{aligned} \tag{3}$$

2

For the structured I/O analysis, we will approximate $\mathbf{u}$ in $\mathbf{u}_\gamma$ as a structured uncertainty and thus, neglect the dependence of $\mathbf{u}_\gamma$ on the velocities and consequently, the nonlinear coupling between $\mathbf{y}$ and $\mathbf{u}$. This is a useful approximation since prior studies have published results that were in agreement with direct numerical simulations (DNS) using this approach [10]. We will refer to the approximation of $\mathbf{u}_\gamma$ as Δ_r, which is defined as

$$\Delta_r = \mathrm{diag}(-\mathbf{u}_\xi^{\mathrm{T}}, -\mathbf{u}_\xi^{\mathrm{T}}, -\mathbf{u}_\xi^{\mathrm{T}}) \tag{4}$$

where $\mathbf{u}_\xi$ is the approximation of $\mathbf{u}$. Then, the system in (3) can be envisioned as a feedback interconnection between a linear system $\mathcal{G}$ and Δ_r, as shown in fig. 1. Thus, the signal $\mathbf{f}$ is characterized as a forcing to the system, which gets mapped from the outputs $\mathbf{y}$ through Δ_r i.e., $\mathbf{f} = \Delta_r \mathbf{y}$. Next, using the equations given in (3), we will construct a frequency-based operator that will allow for I/O analysis.
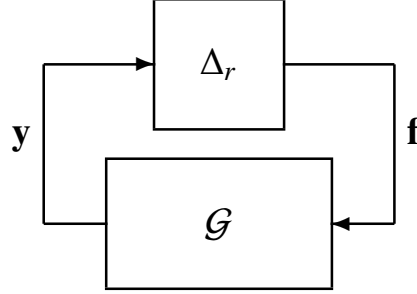

Fig. 1   Feedback representation of the Navier-Stokes system.

B. Numerical Discretization

In this section, we briefly describe the numerical discretization of the system $\mathcal{G}$ to construct an I/O frequency-based operator. We will use the spatially-discretized velocity-vorticity representation of equation (3) for all computations [14]. Thus, $\mathcal{G}$ is spatially-discretized using a truncated set of Fourier-Chebyshev-Fourier basis functions of the form:

$$\mathbf{u} = \hat{\mathbf{u}}(y)e^{\mathbf{i}(\kappa_x x + \kappa_z z + \omega t)} \tag{5}$$

where $\hat{(\cdot)}$ represents the discrete operator, $\mathbf{i} = \sqrt{-1}$ is the imaginary unit, $\hat{\mathbf{u}}(y)$ is the Fourier coefficient discretized in the y-direction using the Chebyshev basis, κ_x and κ_z are the Fourier wavenumbers in the respective x and z directions, and ω is the frequency. To obtain the velocity-vorticity representation of NSE, we project equations in (3) onto a divergence-free subspace, where the pressure dependence is removed by taking the Laplacian of the y-momentum and using the incompressibility condition. Thus, we evaluate the system in a projected space with only wall-normal velocity (v) and vorticity (η_y) as the evolution states. Additionally, we assume a streamwise baseflow that is y dependent, i.e., $\mathbf{U}_b = [U(y),\ 0,\ 0]^{\mathrm{T}}$. The spatially-discretized velocity-vorticity formulation of $\mathcal{G}$ results as:

$$\begin{aligned}
\mathbf{i}\omega\hat{\mathbf{x}} &= \hat{\mathbf{A}}(\kappa_x, \kappa_z)\hat{\mathbf{x}} + \hat{\mathbf{B}}(\kappa_x, \kappa_z)\hat{\mathbf{f}} \\
\hat{\mathbf{y}} &= \mathrm{diag}(\hat{\nabla}, \hat{\nabla}, \hat{\nabla})\hat{\mathbf{C}}(\kappa_x, \kappa_z)\hat{\mathbf{x}} = \hat{\bar{\bar{\nabla}}}\hat{\mathbf{C}}\hat{\mathbf{x}}
\end{aligned} \tag{6}$$

where $\hat{\mathbf{x}} = \begin{bmatrix} \hat{v}^{\mathrm{H}}, & \hat{\eta}_y^{\mathrm{H}} \end{bmatrix}^{\mathrm{H}} \in \mathbb{C}^k$ is the evolution state given by the discrete wall-normal velocity ($\hat{v}$) and vorticity ($\hat{\eta}_y$), and $\hat{\nabla} = [\mathbf{i}\kappa_x, \partial_y, \mathbf{i}\kappa_z]^{\mathrm{T}}$ is the discrete gradient operator. Moreover, $\hat{\mathbf{A}}(\kappa_x, \kappa_z) \in \mathbb{C}^{k \times k}$, $\hat{\mathbf{B}}(\kappa_x, \kappa_z) \in \mathbb{C}^{k \times m}$ and $\hat{\mathbf{C}}(\kappa_x, \kappa_z) \in \mathbb{C}^{l \times k}$ are the system matrices, defined as:

$$\hat{\mathbf{A}}(\kappa_x, \kappa_z) = \begin{bmatrix} \hat{\nabla}^2 & 0 \\ 0 & \mathbf{I} \end{bmatrix}^{-1} \begin{bmatrix} -\mathbf{i}\kappa_x U \hat{\nabla}^2 + \mathbf{i}\kappa_x U'' + \hat{\nabla}^4/Re & 0 \\ -\mathbf{i}\kappa_z U' & -\mathbf{i}\kappa_x U + \hat{\nabla}^2/Re \end{bmatrix},$$

$$\hat{\mathbf{B}}(\kappa_x, \kappa_z) = \begin{bmatrix} \hat{\nabla}^2 & 0 \\ 0 & \mathbf{I} \end{bmatrix}^{-1} \begin{bmatrix} -\mathbf{i}\kappa_x \partial_y & -(\kappa_x^2 + \kappa_z^2) & -\mathbf{i}\kappa_z \partial_y \\ \mathbf{i}\kappa_z & 0 & -\mathbf{i}\kappa_x \end{bmatrix},$$

$$\hat{\mathbf{C}}(\kappa_x, \kappa_z) = \frac{1}{\kappa_x^2 + \kappa_z^2} \begin{bmatrix} \mathbf{i}\kappa_x \partial_y & -\mathbf{i}\kappa_z \\ \kappa_x^2 + \kappa_z^2 & 0 \\ \mathbf{i}\kappa_z \partial_y & \mathbf{i}\kappa_x \end{bmatrix},$$

3

where $U'' = \partial_{yy}U(y)$, $U' = \partial_y U(y)$, $\hat{\nabla}^2 = -\kappa_x^2 - \kappa_z^2 + \partial_{yy}$ and $\hat{\nabla}^4 = \partial_{yyyy} - 2(\kappa_x^2 + \kappa_z^2)\partial_{yy} + (\kappa_x^2 + \kappa_z^2)^2$. Thus, using the equations in (6), we compute an input-output frequency operator $\mathbf{M}(\omega, \kappa_x, \kappa_z) = \hat{\nabla}\hat{\mathbf{C}}(\kappa_x, \kappa_z)(\mathbf{i}\omega\mathbf{I}_k - \hat{\mathbf{A}}(\kappa_x, \kappa_z))^{-1}\hat{\mathbf{B}}(\kappa_x, \kappa_z)$ such that $\hat{\mathbf{f}} = \mathbf{M}\hat{\mathbf{y}}$. Then, the I/O stability is determined using $\mathbf{M}(\omega, \kappa_x, \kappa_z)$ over a grid of frequencies and wavenumbers. Note that $\mathbf{M}(\omega, \kappa_x, \kappa_z)$ is the frequency response of a linear time-invariant (LTI) system. For a fixed wavenumber-frequency triplet $(\kappa_x, \kappa_z, \omega)$, $\mathbf{M}(\omega, \kappa_x, \kappa_z)$ is simply a fixed complex matrix $\mathbf{M} \in \mathbb{C}^{n\times m}$. Consequently, $\hat{\Delta}_r \in \mathbb{C}^{m\times n}$ is also a complex matrix, where $\hat{\mathbf{u}}_\xi \in \mathbb{C}^{n_1 \times m_1}$ is the discretized version of $\mathbf{u}_\xi$, and $n = 3n_1$ and $m = 3m_1$. Consequently, the forcing inputs and system outputs are $\hat{\mathbf{f}} \in \mathbb{C}^m$ and $\hat{\mathbf{y}} \in \mathbb{C}^n$, where m and n are the number of inputs and outputs of (6), respectively. Going forward, we will describe the methods for computing the I/O stability of a complex matrix $\mathbf{M}$. The extension to the LTI case is based on gridding over ω. We note that the I/O signals and states in (6) are transformed into a coordinate system, where the inner-product of the I/O signals represents the $\mathcal{L}_2$ norm of square-integrable functions and the inner product of the evolution states is the kinetic energy [15]. Thus, we have the following equations:

$$\tilde{\mathbf{y}} = \mathbf{W}_1^{-\frac{1}{2}}\hat{\mathbf{y}}, \ \ \tilde{\mathbf{f}} = \mathbf{W}_2^{-\frac{1}{2}}\hat{\mathbf{f}}, \ \ \tilde{\mathbf{x}} = \mathbf{E}^{-\frac{1}{2}}\hat{\mathbf{x}} \tag{7}$$

where $\mathbf{W}_1 \in \mathbb{C}^{n\times n}$ and $\mathbf{W}_2 \in \mathbb{C}^{m\times m}$ are the quadrature weights computed using the definition of an inner product of a square-integrable function [16], and $\mathbf{E} \in \mathbb{C}^{k\times k}$ is the kinetic energy quadrature obtained from the kinetic energy definition of a fluid flow [17]. Note that $(\tilde{\cdot})$ notation defines the non-transformed vectors. The numerical implementation for computing the quadrature weights uses the Clenshaw-Curtis quadrature method given in algorithm "clencurt.m" of [16]. For computing the kinetic energy quadrature, see section 4.2.1 of [17].

III. Structured Input-Output Analysis

In this section, we will discuss the methods for computing the I/O gains and mode shapes of a complex matrix $\mathbf{M} \in \mathbb{C}^{n\times m}$ given a structured $\hat{\Delta} \in \mathbb{C}^{m\times n}$. We first note that $\hat{\Delta}$ for a given system belongs to a set of structured, complex matrices $\hat{\mathbf{\Delta}} \subseteq \mathbb{C}^{m\times n}$. In the context of incompressible fluid flows, $\hat{\Delta} \in \hat{\mathbf{\Delta}}_r$, where $\hat{\mathbf{\Delta}}_r := \{\hat{\Delta} = \mathbf{I}_v \otimes \hat{\Delta}_1 : \hat{\Delta}_1 \in \mathbb{C}^{m_1 \times n_1}\} \subset \mathbb{C}^{m\times n}$ is a set of repeated structured uncertainty [13]. Here $\otimes$ denotes a Kronecker product. We will exploit the structure of $\hat{\Delta}$ to compute the structured I/O gain values (SSV) and I/O mode shapes to obtain useful insights into the modal behavior of the system. Additionally, we will show that the computation of the lower bound of $\mu(\mathbf{M})$ also yields the I/O mode shapes, i.e., $\hat{\mathbf{y}}$ and $\hat{\mathbf{f}}$. Next, we will describe the methods to compute the SSV and consequently, the mode shapes.

A. Structured Singular Values

Consider the case for the matrix $\mathbf{M} \in \mathbb{C}^{n\times m}$. The SSV is defined for a given structured $\hat{\Delta} \in \mathbb{C}^{m\times n}$ as

$$\mu_{\hat{\mathbf{\Delta}}}(\mathbf{M}) = \frac{1}{\min(\|\hat{\Delta}\|_2 : \hat{\Delta} \in \hat{\mathbf{\Delta}}, \det(\mathbf{I}_n - \mathbf{M}\hat{\Delta}) = 0)} \tag{8}$$

where $\mathbf{I}_n \in \mathbb{R}^{n\times n}$ is an identity matrix and $\|\cdot\|_2$ is the 2-norm. If there does not exist $\hat{\Delta} \in \hat{\mathbf{\Delta}}$ such that $\det(\mathbf{I}_n - \mathbf{M}\hat{\Delta}) = 0$, then $\mu_{\hat{\mathbf{\Delta}}}(\mathbf{M}) = 0$. We will omit the subscript $\hat{\mathbf{\Delta}}$ in (8) when the structure of $\hat{\Delta}$ is clear. It follows that the SSV computed using (8) is obtained for the smallest $\hat{\Delta}$ such that $\mathbf{I}_n - \mathbf{M}\hat{\Delta}$ is singular. Hence, there exist signals $\hat{\mathbf{f}} \in \mathbb{C}^m$ and $\hat{\mathbf{y}} \in \mathbb{C}^n$ such that $\hat{\mathbf{y}} = \mathbf{M}\hat{\mathbf{f}}$ and $\hat{\mathbf{f}} = \hat{\Delta}\hat{\mathbf{y}}$, which define the feedback interconnection shown in figure 1 (see Remark 3.4 in [18] for more details). Recall that SSVs represent the worst-case I/O amplification of a system and therefore, inversely relate to the stability margin [19]. Thus, it follows from the small gain theorem that a large SSV for a system indicates a small stability margin, or in other words, the system is sensitive to small perturbations that can trigger instabilities and vice versa [19, 20].

Computing $\mu(\mathbf{M})$ for a generic is an NP-Hard problem [21–23]. As such, the exact value of $\mu(\mathbf{M})$ is not guaranteed for every structured $\hat{\Delta}$. However, approximate solutions to (8) are possible and have been studied in [24] for various $\hat{\Delta}$. Solution approaches for the specific structure of interest for incompressible flows was addressed in [13]. The general solution involves exploiting the structure of $\hat{\Delta}$ to obtain upper and lower bounds on $\mu(\mathbf{M})$, which requires the use of numerical algorithms. The gap between the upper and lower bound determines the quality of the solution to $\mu(\mathbf{M})$. However, for some structures of $\hat{\Delta}$, as noted in the works of [18, 25, 26], exact value of SSV can be computed. Next, we briefly describe frameworks for obtaining these upper and lower bounds on $\mu(\mathbf{M})$.

1. Upper Bounds

In this section, we briefly describe the framework for computing the upper bound on $\mu(\mathbf{M})$. We first note that for each set of structured uncertainty $\hat{\Delta}$, there are sets of commuting "non-singular" matrices $\mathcal{D}_1$ and $\mathcal{D}_2$. The solution to the approximate upper bound problem involves computing a set of commuting matrices such that $\mathbf{D}_2\hat{\Delta} = \hat{\Delta}\mathbf{D}_1$, where $\mathbf{D}_1 \in \mathcal{D}_1$ and $\mathbf{D}_2 \in \mathcal{D}_2$. The commuting matrices are transformations on $\mathbf{M}$ such that they do not change the value of $\mu(\mathbf{M})$, but serve to refine the upper bound estimate [18]. Thus, we get an upper bound $\mu(\mathbf{M}) \leq \alpha$ such that $\alpha := \min \|\mathbf{D}_1\mathbf{M}\mathbf{D}_2^{-1}\|_2$. This is known as the D-scale upper bound problem, which can be formulated into a convex optimization problem to solve for $\mathbf{D}_1$ and $\mathbf{D}_2$ [24]. Thus, the structure of the commuting matrices is used to impose the structure of $\hat{\Delta}$. An equivalent generalized eigenvalue problem (GEVP) for α can be formulated for minimizing the maximum singular value of $\mathbf{D}_1\mathbf{M}\mathbf{D}_2^{-1}$ as

$$
\begin{aligned}
&\min \alpha^2 \\
&\text{subject to: } \mathbf{M}^{\mathrm{H}}\mathbf{X}_1\mathbf{M} < \alpha^2\mathbf{X}_2, \\
&\qquad\qquad \mathbf{X}_1 > 0, \mathbf{X}_2 > 0
\end{aligned}
\tag{9}
$$

where $\mathbf{X}_1 = \mathbf{D}_1^{\mathrm{H}}\mathbf{D}_1$ and $\mathbf{X}_2 = \mathbf{D}_2^{\mathrm{H}}\mathbf{D}_2$, and $\mathbf{D}_1 \in \mathbb{C}^{n \times n}$ and $\mathbf{D}_2 \in \mathbb{C}^{m \times m}$. For incompressible flows, we have $\hat{\Delta} \in \hat{\Delta}_r$ and thus, $\hat{\Delta}$ has the structure given in (4). Then, $\mathbf{D}_1 \in \mathcal{D}_{r_1}$ and $\mathbf{D}_2 \in \mathcal{D}_{r_2}$, where $\mathcal{D}_{r_1} := \{\mathbf{S} \otimes \mathbf{I}_{n_1} : \mathbf{S} \in \mathbb{C}^{3 \times 3}, \det(\mathbf{S}) \neq 0\}$ and $\mathcal{D}_{r_2} := \{\mathbf{S} \otimes \mathbf{I}_{m_1} : \mathbf{S} \in \mathbb{C}^{3 \times 3}, \det(\mathbf{S}) \neq 0\}$ are the sets of commuting matrices. Hence, $\mathbf{X}_1 = \mathbf{S}^{\mathrm{H}}\mathbf{S} \otimes \mathbf{I}_{n_1} = \mathbf{R} \otimes \mathbf{I}_{n_1}$ and $\mathbf{X}_2 = \mathbf{S}^{\mathrm{H}}\mathbf{S} \otimes \mathbf{I}_{m_1} = \mathbf{R} \otimes \mathbf{I}_{m_1}$, where $\mathbf{R} \in \mathbb{C}^{3 \times 3}$ is Hermitian, and $\mathbf{I}_{n_1} \in \mathbb{R}^{n_1 \times n_1}$ and $\mathbf{I}_{m_1} \in \mathbb{R}^{m_1 \times m_1}$ are the identity matrices. Finally, the upper bound problem for $\hat{\Delta} \in \hat{\Delta}_r$ will be the following:

$$
\begin{aligned}
&\min_{\mathbf{R}=\mathbf{R}^{\mathrm{H}} \in \mathbb{C}^{3 \times 3}} \alpha^2 \\
&\text{subject to: } \mathbf{M}^{\mathrm{H}}\mathbf{X}_1\mathbf{M} < \alpha^2\mathbf{X}_2, \\
&\qquad\qquad \mathbf{R} > 0.
\end{aligned}
\tag{10}
$$

Since $\mathbf{R}$ is scale invariant for any scalar $c > 0$, we can replace $\mathbf{R} > 0$ in (10) with $\mathbf{I}_3 \leq \mathbf{R} \leq r_{cond}\mathbf{I}_3$ to improve the numerical conditioning, where r_{cond} is the condition number. We will use the method of centers algorithm as described in Algorithm 1 of [13] to compute α from (10) for the incompressible flow discussed in the later sections.

Note that the formulation of the upper bound problem in (9) is not restricted to the structured $\hat{\Delta}$ presented in this paper. We can solve (9) for any complex structured matrix $\hat{\Delta}$, given the appropriate structure of the associated scaling matrices. For example, the original formulation of structured I/O for incompressible flows in [10] approximates $\mathbf{u}_\gamma$ with non-repeated entries, i.e., $\hat{\Delta}_{nr} = \mathrm{diag}(-\hat{\mathbf{u}}_{\xi,1}^{\mathrm{T}}, -\hat{\mathbf{u}}_{\xi,2}^{\mathrm{T}}, -\hat{\mathbf{u}}_{\xi,3}^{\mathrm{T}})$, where $\hat{\mathbf{u}}_{\xi,i} \in \mathbb{C}^{n_i \times m_i}$ for $i = 1 \dots 3$, and $n = \sum_{i=1}^3 n_i$ and $m = \sum_{i=1}^3 m_i$. Then, $\mathbf{D}_1 = \mathrm{diag}(d_1\mathbf{I}_n, d_2\mathbf{I}_m, d_3\mathbf{I}_{n_3})$ and $\mathbf{D}_2 = \mathrm{diag}(d_1\mathbf{I}_{m_1}, d_2\mathbf{I}_{m_2}, d_3\mathbf{I}_{m_3})$, where $d_i \in \mathbb{R}_{>0}$ are scalars, and $\mathbf{I}_{n_i} \in \mathbb{R}^{n_i \times n_i}$ and $\mathbf{I}_{m_i} \in \mathbb{R}^{m_i \times m_i}$ are the identity matrices. We note that for $\hat{\Delta}_{nr}$, there is an already existing fast algorithm for upper bound computations known as the Osborne's iteration [27]. However, Osborne's iteration uses a conservative Frobenius norm bound to solve for the upper bound i.e., $\mu(\mathbf{M}) \leq \min \|\mathbf{D}_1\mathbf{M}\mathbf{D}_2^{-1}\|_2 \leq \min \|\mathbf{D}_1\mathbf{M}\mathbf{D}_2^{-1}\|_{\mathrm{F}}$. Thus, Osborne's iteration may not yield the best upper bound estimates. [13, 27] for more details). It is important to realize that the least conservative bound for $\hat{\Delta}_{nr}$ is obtained by solving (9).

Furthermore, we would like to note that when the gap between the upper and lower bounds is tight—e.g., less than 1%—then, the mode shapes can be computed using the SVD of the scaled operator $\mathbf{D}_1\mathbf{M}\mathbf{D}_2^{-1}$. In that case, the mode shapes from the upper-bound calculation will be converged and have physical meaning. Thus, we can compute those mode shapes as

$$
\begin{aligned}
\hat{\mathbf{y}} &= \mathbf{D}_1^{-1}\mathbf{U}_1 \\
\hat{\mathbf{f}} &= \mathbf{D}_2^{-1}\mathbf{V}_1
\end{aligned}
\tag{11}
$$

where $\mathbf{U}_1$ and $\mathbf{V}_1$ are the left and right unitary vectors associated with the largest singular value of $\mathbf{D}_1\mathbf{M}\mathbf{D}_2^{-1}$.

2. Lower Bounds and Input-Output Signals

In this section, we describe a generalized power-iteration that optimizes over the I/O signals $\hat{\mathbf{y}}$ and $\hat{\mathbf{f}}$ to compute the mode shapes and a lower bound on $\mu(\mathbf{M})$ for a given $\hat{\Delta} \in \mathbb{C}^{m \times n}$. Recall that the exact value of $\mu(\mathbf{M})$ is obtained for the smallest possible $\hat{\Delta}$ that satisfies $\det(\mathbf{I}_n - \mathbf{M}\hat{\Delta}) = 0$. Hence, the power-iteration attempts to find the smallest $\hat{\Delta}$ so that

$\mathbf{I}_n - \mathbf{M}\hat{\Delta}$ is singular, which is equivalent to finding the signals $\hat{\mathbf{y}} \in \mathbb{C}^n$ and $\hat{\mathbf{f}} \in \mathbb{C}^m$ such that $\hat{\mathbf{y}} = \mathbf{M}\hat{\mathbf{f}}$ and $\hat{\mathbf{f}} = \hat{\Delta}\hat{\mathbf{y}}$. In general, the iteration does not compute the smallest $\hat{\Delta}$ and thus, only yields a lower bound on $\mu(\mathbf{M})$. Therefore, the power-iteration implicitly solves for the lower bound β given by the maximization problem, $\beta := \max \rho(\hat{\Delta}\mathbf{M})$, where ρ is the spectral radius of a matrix [28]. Thus, the lower bound provides a sufficient condition for instability of the system [12, 18, 28–30]. The work in [18] provides a comprehensive review of power-iteration methods for several $\hat{\Delta}$ block structures to compute the lower bounds and the associated I/O signals. Interestingly, the specific case of interest $Delta \in \Delta_r$ was never considered until recently in [13]. The power-iteration presented in [13] generalizes the method in [18], as described next.

To describe the power-iteration, we first define the following reshaping function $L_{n_1} : \mathbb{C}^{3n_1} \to \mathbb{C}^{n_1 \times 3}$:

$$\mathbf{y} = \begin{bmatrix} \mathbf{y}_1 \\ \mathbf{y}_2 \\ \mathbf{y}_3 \end{bmatrix} \in \mathbb{C}^{3n_1} \text{ maps to } L_{n_1}(\mathbf{y}) = \begin{bmatrix} \mathbf{y}_1, \mathbf{y}_2, \mathbf{y}_3 \end{bmatrix}. \tag{12}$$

This operation restacks the partitioned vector $\hat{\mathbf{y}} \in \mathbb{C}^{3n_1}$ into a matrix. The inverse $L_{n_1}^{-1}$ will convert the matrix back to a column vector. The operation $L_{m_1} : \mathbb{C}^{3m_1} \to \mathbb{C}^{m_1 \times 3}$ is defined similarly on vectors $\hat{\mathbf{f}} \in \mathbb{C}^{3m_1}$. The relation $\hat{\mathbf{f}} = \hat{\Delta}\hat{\mathbf{y}}$ is equivalent to $L_{m_1}(\hat{\mathbf{f}}) = -\hat{\mathbf{u}}_\xi L_{n_1}(\hat{\mathbf{y}})$. Additionally, we define a function $\mathbf{Q}(\mathbf{G})$ such that for any given matrix $\mathbf{G} = \mathbf{U}\mathbf{\Sigma}\mathbf{V}^{\mathrm{H}}$, $\mathbf{Q}(\mathbf{G}) = \mathbf{U}\mathbf{V}^{\mathrm{H}}$, where $\mathbf{U} \notin \ker(\mathbf{G}^{\mathrm{H}})$ and $\mathbf{V} \notin \ker(\mathbf{G})$ are unitary left and right matrices, respectively, and $\mathbf{\Sigma}$ is a matrix of non-zero singular values. Note that $\sigma_{max}(\mathbf{Q}(\mathbf{G})) = 1$. Finally, the power-iteration for some $\beta > 0$ is defined as:

$$\beta\hat{\mathbf{a}} = \mathbf{M}\hat{\mathbf{b}}, \tag{13a}$$

$$L_{n_1}(\hat{\mathbf{z}}) = \mathbf{Q}\left(L_{n_1}(\hat{\mathbf{a}})L_{m_1}(\hat{\mathbf{w}})^{\mathrm{H}}\right) L_{m_1}(\hat{\mathbf{w}}), \tag{13b}$$

$$\beta\hat{\mathbf{w}} = \mathbf{M}^{\mathrm{H}}\hat{\mathbf{z}}, \tag{13c}$$

$$L_{m_1}(\hat{\mathbf{b}}) = \mathbf{Q}\left(L_{m_1}(\hat{\mathbf{w}})L_{n_1}(\hat{\mathbf{a}})^{\mathrm{H}}\right) L_{n_1}(\hat{\mathbf{a}}). \tag{13d}$$

Simply iterating over the equations (13a) - (13d) starting from any initial unit norm vector $\hat{\mathbf{b}}$ and $\hat{\mathbf{w}}$ corresponds to the standard power-iteration to compute $\sigma_{max}(\mathbf{M})$. For incompressible flows, we have $\hat{\Delta} \in \hat{\Delta}_r$, so we define $\hat{\mathbf{f}} = \hat{\mathbf{b}}$, $\hat{\mathbf{y}} = \beta\hat{\mathbf{a}}$ and $\hat{\Delta} := \mathbf{I}_3 \otimes \frac{1}{\beta}\mathbf{Q}\left(L_{m_1}(\hat{\mathbf{w}})L_{n_1}(\hat{\mathbf{a}})^{\mathrm{H}}\right)$ as the forcing modes, response modes and structured uncertainty, respectively. Then, (13a) and (13d) are equivalent to $\hat{\mathbf{y}} = \mathbf{M}\hat{\mathbf{f}}$ and $\hat{\mathbf{f}} = \hat{\Delta}\hat{\mathbf{y}}$ given in fig. 1. The resulting β from the power-iteration is the lower bound on $\mu(\mathbf{M})$ for $\hat{\Delta} \in \hat{\Delta}_r$. We will use the parameters defined for the power-iteration in Algorithm 3 of [13] to compute the lower bounds and mode shapes. Recall from (6) that $\hat{\mathbf{f}}$ is simply the nonlinear forcing signal and the outputs $\hat{\mathbf{y}}$ are the gradients of velocities. Thus, to compute the velocities, we must take the inverse of gradients, i.e., $\hat{\mathbf{u}} = \mathrm{diag}(\hat{\nabla}, \hat{\nabla}, \hat{\nabla})^{-1}\mathbf{W}_1^{-\frac{1}{2}}\hat{\mathbf{y}}$. Similar to the case of upper bounds, different $\hat{\Delta}$ structures can be used for the power-iteration given by (13a) - (13d), such as $\hat{\Delta}_{nr} = \mathrm{diag}(-\hat{\mathbf{u}}_{\xi,1}^{\mathrm{T}}, -\hat{\mathbf{u}}_{\xi,2}^{\mathrm{T}}, -\hat{\mathbf{u}}_{\xi,3}^{\mathrm{T}})$ from [10]. Then, we would get the following equations:

$$\beta\hat{\mathbf{a}} = \mathbf{M}\hat{\mathbf{b}} \tag{14a}$$

$$\hat{\mathbf{z}}_1 = \frac{\|\hat{\mathbf{w}}_1\|_2}{\|\hat{\mathbf{a}}_1\|_2}\hat{\mathbf{a}}_1, \;\; \hat{\mathbf{z}}_2 = \frac{\|\hat{\mathbf{w}}_2\|_2}{\|\hat{\mathbf{a}}_2\|_2}\hat{\mathbf{a}}_2, \;\; \hat{\mathbf{z}}_3 = \frac{\|\hat{\mathbf{w}}_3\|_2}{\|\hat{\mathbf{a}}_3\|_2}\hat{\mathbf{a}}_3 \tag{14b}$$

$$\beta\hat{\mathbf{w}} = \mathbf{M}^{\mathrm{H}}\hat{\mathbf{z}} \tag{14c}$$

$$\hat{\mathbf{b}}_1 = \frac{\|\hat{\mathbf{a}}_1\|_2}{\|\hat{\mathbf{w}}_1\|_2}\hat{\mathbf{w}}_1, \;\; \hat{\mathbf{b}}_2 = \frac{\|\hat{\mathbf{a}}_2\|_2}{\|\hat{\mathbf{w}}_2\|_2}\hat{\mathbf{w}}_2, \;\; \hat{\mathbf{b}}_3 = \frac{\|\hat{\mathbf{a}}_3\|_2}{\|\hat{\mathbf{w}}_3\|_2}\hat{\mathbf{w}}_3 \tag{14d}$$

.

where $\hat{\mathbf{a}}_i, \hat{\mathbf{z}}_i, \hat{\mathbf{b}}_i, \hat{\mathbf{w}}_i \in \mathbb{C}^{m_i}$ are compatibly partitioned signals for $i = 1 \ldots 3$. Iterating through equations (14a) - (14d) would yield a power-iteration for the lower bound on $\mu(\mathbf{M})$ given $\hat{\Delta}_{nr}$. Note that (14d) gives $\|\hat{\mathbf{b}}_i\|_2 = \|\hat{\mathbf{a}}_i\|_2$ for $i = 1 \ldots 3$. Thus, there exists $\mathbf{Q}_i \in \mathbb{C}^{m_i \times n_i}$ such that $\|\mathbf{Q}_i\|_2 = 1$ and $\hat{\mathbf{b}}_i = \mathbf{Q}_i\hat{\mathbf{a}}_i$. Then, define $\hat{\mathbf{f}} = \hat{\mathbf{b}}$, $\hat{\mathbf{y}} = \beta\hat{\mathbf{a}}$ and $\hat{\Delta}_{nr} = \frac{1}{\beta}\mathrm{diag}(\mathbf{Q}_1, \mathbf{Q}_2, \mathbf{Q}_3)$ as the forcing modes, response modes and structured uncertainty of the system, respectively. It can be verified from (14a) that $\hat{\mathbf{y}} = \mathbf{M}\hat{\mathbf{f}}$.

6

IV. Results

In this section, we compute the SSV bounds and I/O signals using the methods described in the previous sections for a channel flow system (see fig. 2). Thus, we will use $\hat{\Delta}_r$ as the structured uncertainty of the system for all computations related to the SSV upper and lower bounds. We use $Re = 690$ and a parabolic baseflow $U(y) = 1 - y^2$ for the analysis problem, where $y \in (-1, \ 1)$. Furthermore, we choose a $50 \times 90 \times 200$ grid of $n_{\kappa_x} \times n_{\kappa_z} \times n_\omega$ to compute the bounds on
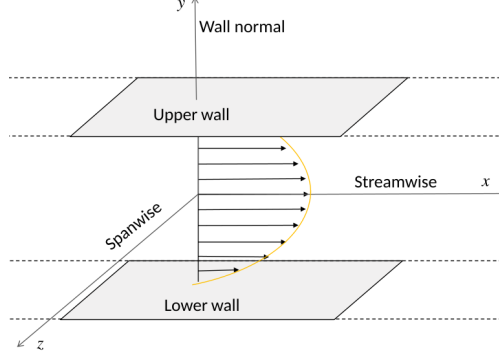
Fig. 2   Channel Flow

$\mu(\mathbf{M})$, where n_{κ_x}, n_{κ_z} and n_ω are the total grid points for κ_x, κ_z and ω, respectively. The values are logrithmically spaced $\kappa_x = [10^{-4}, \ 10^{0.48}]$, $\kappa_z = [10^{-2}, \ 10^{1.2}]$ and $\omega = [-10^{1.5}, \ 10^{1.5}]$. The points in y-direction are computed as $y_i = cos(i\pi/N_y)$ for $i = 1, \ldots, N_y$, where N_y are the total Chebyshev collocation points excluding the channel walls [14]. We choose $N_y = 30$ for the SSV analysis and plotting the mode shapes. Computations per wavenumber-frequency triplet $(\kappa_x, \kappa_z, \omega)$ take 1.1 and 0.09 seconds for upper and lower bounds on an ASUS ROG M15 laptop with a 6 core Intel 2.6 GHz i7-10750H CPU, 16 GB RAM and an RTX 2070 Max-Q GPU, respectively. We use the MATLAB *parfor* command for calculating the SSV bounds with parallel computing. The *parfor* is used on the frequency grid so that the computations on the wavenumber grid run in parallel.

The bounds on the SSV are compared against the H_∞ values of $\mathbf{M}(\omega, \kappa_x, \kappa_z)$ to showcase the difference in I/O gain values when there is a structured Δ_r associated with the fluid system. The H_∞ analysis assumes an unstructured uncertainty on the system, i.e., $\hat{\Delta}_{us} \in \mathbb{C}^{m \times n}$, where $\hat{\Delta}_{us}$ is a full complex matrix. Consequently, the forcing signal $\hat{\mathbf{f}}$ is also unstructured, which is different than the one used in the SSV analysis [15]. However, the outputs between the H_∞ and SSV analysis are the same. For the LTI system $\mathbf{M}(\omega, \kappa_x, \kappa_z)$, the SSV upper and lower bound for a given wavenumber pair (κ_x, κ_z) and the associated range of frequencies ω is computed as $\alpha := \max_\omega \{\min_{\mathbf{D}_1 \in \mathcal{D}_{r_1}, \mathbf{D}_2 \in \mathcal{D}_{r_2}} \|\mathbf{D}_1 \mathbf{M}(\omega, \kappa_x, \kappa_z) \mathbf{D}_2^{-1}\|_2\}$ and $\beta := \max_\omega \{\max_{\hat{\Delta}_r \in \mathbb{C}^{m \times n}} \rho(\hat{\Delta}_r \mathbf{M}(\omega, \kappa_x, \kappa_z))\}$. Similarly, the H_∞ values are computed as $\|\mathbf{M}(\omega, \kappa_x, \kappa_z)\|_\infty = \max_\omega \|\mathbf{M}(\omega, \kappa_x, \kappa_z)\|_2$. The computed upper and lower bound of SSV are shown in fig. 3 along with the H_∞ values for $\mathbf{M}(\omega, \kappa_\mathbf{x}, \kappa_\mathbf{z})$.

The overall magnitude of the SSV bounds is small as compared to the H_∞ gain values. The key difference between the two I/O gain methods is that the SSV computations use the structure of $\hat{\Delta}_r$ as opposed to the H_∞ method, which approximates $\hat{\Delta}_r$ with an unstructured full complex matrix $\hat{\Delta}_{us}$. Additionally, the regions with the largest gain values occur at different wavenumbers for the SSV upper bound and H_∞ analyses. The maximum value for $\|\mathbf{M}(\omega, \kappa_x, \kappa_z)\|_\infty$ occurs at $\kappa_x = 1.5236 \times 10^{-4}$ and $\kappa_z = 1.8415$—which represents a spanwise disturbance—as opposed to $\kappa_x = 0.0055$ and $\kappa_z = 0.0569$ for α—which is an oblique disturbance. Thus, in contrast to the H_∞ analysis, the structured I/O method suggests that the fluid system requires the least amount of energy for transition to turbulence from oblique disturbances. Although a maximal oblique disturbance gain is identified, a continuum of high-gain oblique disturbance scenarios are identified by the structured I/O analysis for $\kappa_x \leq 0.055$ and $\kappa_z \leq 2$ (see fig. 3).. Similar findings were made in direct numerical simulations, where oblique perturbations, i.e., $\kappa_x \approx 1$ and $\kappa_z \approx 1$, require the least amount of energy for flow transition [14, 31]

Recall that the SSV upper bound is inversely related to the stability margin of a system [19]. Thus, the upper bound plot in fig. 3(a) also indicates that the stability margin of the channel flow is greater than anticipated by the H_∞ analysis. More precisely, the H_∞ analysis provides insights similar to the linear stability analysis, where only spanwise perturbations require the least amount of energy i.e., $\kappa_x = 0$ and $\kappa_z \neq 0$ [32]. Furthermore, the lower bound plot has similar values to the upper bound and we can see that the bounds are overall tight, i.e., 98% of the bounds are within less than 5% of each other.

7

In addition to oblique disturbances, the SSV analysis highlights the Tollmien Schlichting (TS) band as seen in the plot of fig. 3(a) for the wavenumber range $\kappa_x = 10^0$ and $\kappa_z = [10^{-2}, 10^0]$, which is not identified as a dominant instability mechanism in the H_∞ analysis. We can plot the modes using power-iteration for the streamwise perturbations as shown in fig. 6 on the Tollmien-Schlichting band, i.e., $(\kappa_x, \kappa_z) = (1, 0)$. We can see that the mode shapes highlight the underlying physics of the TS waves. The velocity and forcing modes in z direction are zero, as TS waves have no direct contribution in that direction. Consequently, the components of vorticity in x and y directions are also zero, which we compute as $\hat{\eta} = \hat{\nabla} \times \hat{\mathbf{u}}$. Note that the v-velocity mode is parabolic with u-velocity shifting from positive to negative across the centerline of the flow. The v-velocity mode shown here occurs in various studies of TS instability, where it is noted to be the unstable eigenmode obtained from the linear analysis [17, 33].
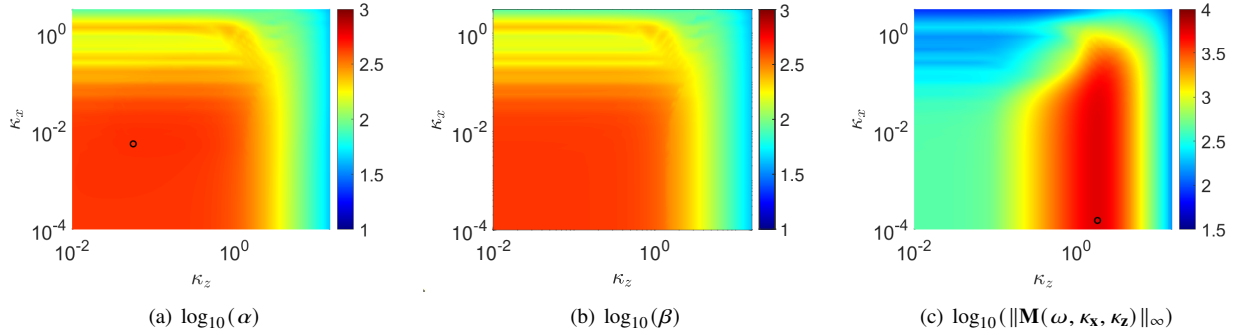

(a) $\log_{10}(\alpha)$ (b) $\log_{10}(\beta)$ (c) $\log_{10}(\|\mathbf{M}(\omega, \kappa_{\mathbf{x}}, \kappa_{\mathbf{z}})\|_\infty)$

Fig. 3   The plots show the distribution of I/O gain values across the wavenumbers. The symbol ($\circ$) on the plot indicates the largest value across the wavenumbers.

(a) Velocity Mode-Shapes   (b) Forcing Mode-Shapes   (c) Vorticity Mode-Shapes
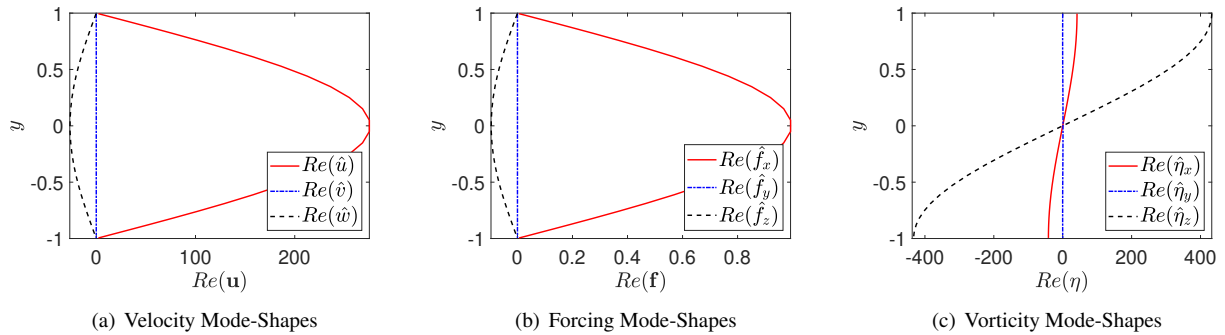
Fig. 4   The plots show the most dominant modes at $\kappa_x = 0.0055$, $\kappa_z = 0.0569$ and $\omega = -0.0046$ computed by power-iteration.

In fig. 4, we plot the mode shapes associated with the peak SSV upper bound value, corresponding to the wavenumber-frequency triplet $\kappa_x = 0.0055$, $\kappa_z = 0.0569$ and $\omega = -0.0046$. The modal plots represent the real parts of forcing, velocity and vorticity. We can see in fig. 4(a) and fig. 4(b) that the velocity and forcing modes have identical shapes i.e., both are parabolic, and u-velocity and f_x-forcing modes are the most dominant. On the contrary, the vorticity varies approximately linearly across the flow domain. In this case, z vorticity is the most dominant mode across the flow domain and has the largest magnitude close to the channel walls. We use the velocity information from these mode shapes to obtain a flow profile at $x = 0$ and $t = 0$. Since the solutions are periodic in x, z and t, the flow profile at any point in x, z and t will only differ by a phase shift. We plot the real data as shown in fig. 9. We can see that there is a large region of high streamwise momentum that is centered between the channel walls with a cross-flow in the spanwise direction as indicated by the arrows. Thus, the destabilizing perturbations for a channel flow are a combination of parabolic streamwise and spanwise perturbations. Additionally, we can infer from the velocity modes that the total streamwise velocity $u = U(y) + \hat{u}(x, y, z, t)$ is also parabolic at the given wavenumbers. Hence, the parabolic base flow itself is the most destabilizing mode when combined with a spanwise perturbation. In fact, the real part of the f_x-forcing mode is exactly the base flow $U(y)$, which is an interesting result.
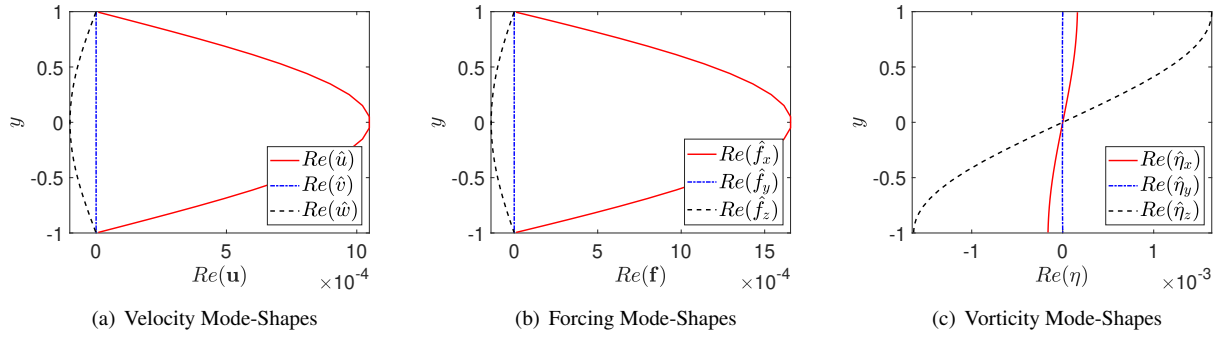
8

(a) Velocity Mode-Shapes   (b) Forcing Mode-Shapes   (c) Vorticity Mode-Shapes

Fig. 5 **The plots show the most dominant modes at** $\kappa_x = 0.0055$**,** $\kappa_z = 0.0569$ **and** $\omega = -0.0046$ **computed using** (11)
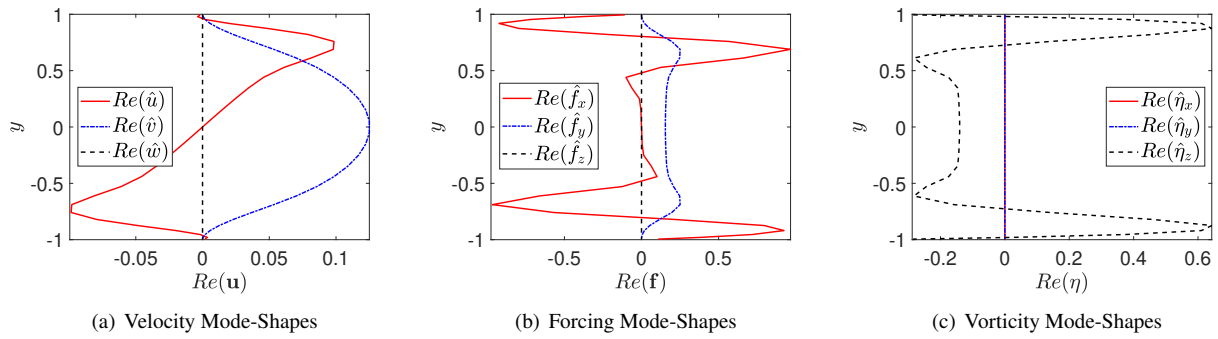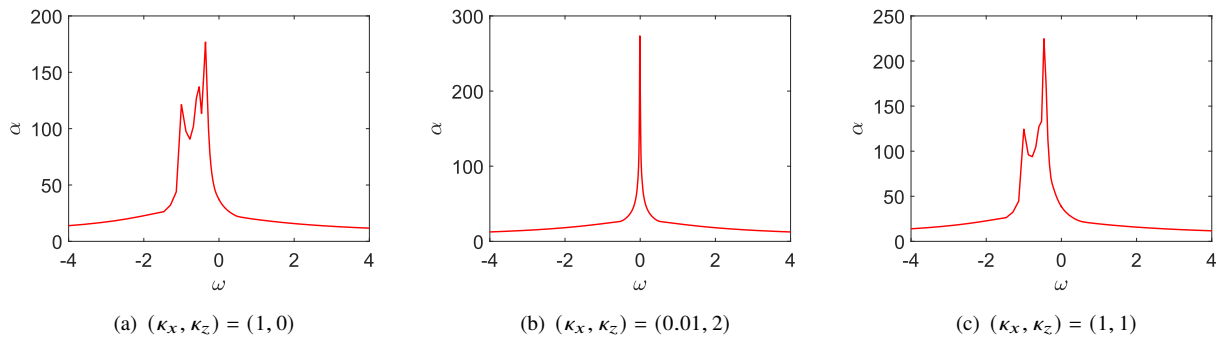

(a) Velocity Mode-Shapes   (b) Forcing Mode-Shapes   (c) Vorticity Mode-Shapes

Fig. 6 **The plots show the most dominant modes at** $\kappa_x = 1$**,** $\kappa_z = 0$ **and** $\omega = -0.3594$ **computed using power iteration**

(a) $(\kappa_x, \kappa_z) = (1, 0)$ (b) $(\kappa_x, \kappa_z) = (0.01, 2)$ (c) $(\kappa_x, \kappa_z) = (1, 1)$

Fig. 7 **The figure shows an upper bound** α **vs frequency plot at each of the wavenumbers.**

9

It is important to note that we can compute the same mode shapes as shown in fig. 4 using equations in (11) on the scaled operator $\mathbf{D}_1\mathbf{M}(\omega, \kappa_x, \kappa_z)\mathbf{D}_2^{-1}$ at $\kappa_x = 0.0055$, $\kappa_z = 0.0569$ and $\omega = -0.0046$. We see in fig. 5 that all the mode shapes match the ones in fig. 4 and they only differ by the values. It is important to realize that these values are arbitrary and therefore, less significant since the relative importance of each mode is similar between the two methods.

Notice that the system at $\omega = -0.0046$ has a steady-state DC behavior. We can see this by looking at the values of the forcing and velocity modes. Given an input forcing as shown in fig. 4(b), all the velocity modes are scaled approximately by a constant gain of 285.2980 at the output. This makes sense since the peak frequency $\omega = -0.0046$ is $O(10^{-3})$ and thus, is close to being zero. We know that a nominally stable system has a steady-state I/O behavior as $\omega \rightarrow 0$, which explains the constant offset between the velocity and forcing mode shapes. Overall, the channel flow system has dominant frequencies closer to zero as shown fig. 8. Additionally, most of the frequencies of the channel flow are biased towards the negative spectrum, which provides insight into the most sensitive direction for perturbations.

Finally, we plot the frequency modes for the wavenumbers $(1, 0)$, $(0.01, 2)$ and $(1, 1)$ in fig. 7, which are most commonly used in literature. We can see that at each of those wavenumbers the most dominant frequencies are close to zero and negative. Thus, it shows that the frequency spectrum of the channel flow for a given wavenumber pair is asymmetric in most cases. Moreover, we also get some secondary frequencies as seen in fig. 7(a) and fig. 7(c) that give us local maximums of the upper bound, which indicate that at certain wavenumbers, there can be multiple frequencies that can excite the channel flow system. Thus, the channel flow system has multiple flow structures that are resonant at multiple frequencies for different combinations of wavenumbers. Although the dominant structures occur at frequencies closest to zero, there are secondary structures at lesser frequencies that can potentially get excited by the nonlinear forcing. This mechanism is most evident when there are streamwise disturbances in the flow as compared to spanwise disturbances.
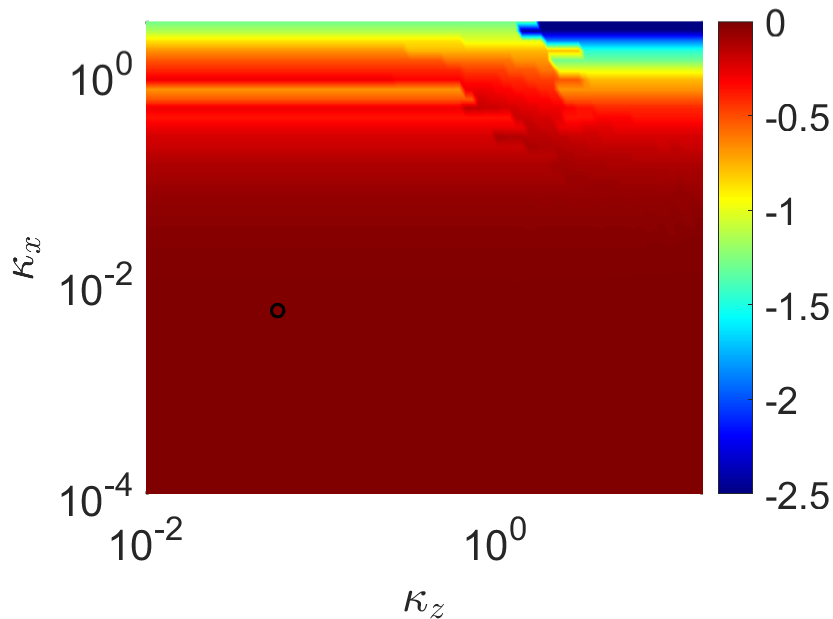

Fig. 8   The figure shows a plot of the associated frequency values for each of the upper bounds α. The symbol ($\circ$) on the plot indicates the wavenumbers for the largest bound α

V. Conclusions

We showed that computing SSV and I/O signals is a useful way of understanding the underlying physics of the flow features and mechanisms that are important in flow transition. Additionally, we demonstrated the methods that can be used to analyze I/O stability of a fluid flow system given a structured uncertainty. We emphasize that the I/O methods explained in this paper can be extended to any LTI system with a complex matrix uncertainty. Furthermore, we found that the SSV upper bound calculations yield the same mechanisms as the power iteration method for the lower bound,
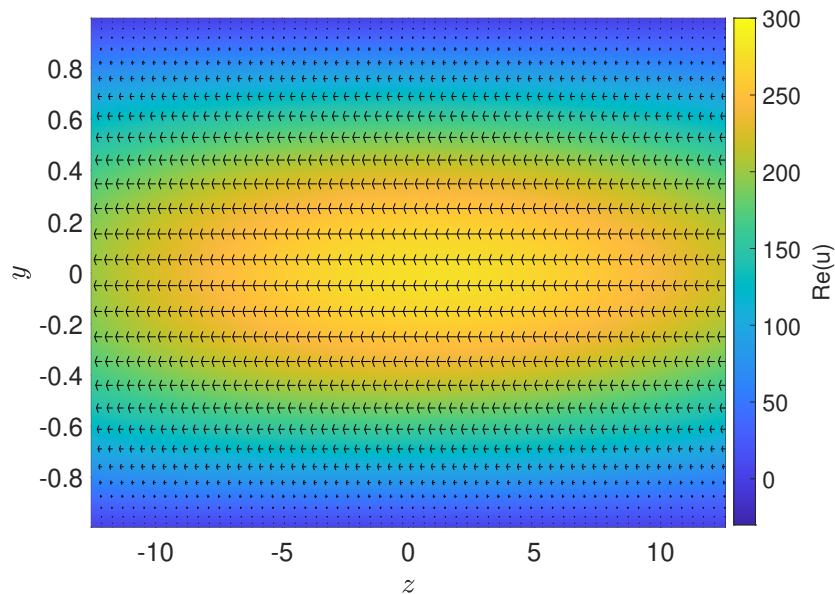
Fig. 9   Flow profile at $x = 0$ **and** $t = 0$ **for** $\kappa_x = 0.0055$ **and** $\kappa_z = 0.0569$**. The contours highlight amplitude of real component of streamwise velocity in the** $y - z$ **plane and the arrows represent vectors for real** $v - w$ **velocity components.**

given the gaps are tight between the bounds. This is a particularly useful result for the case when a given upper bound is known to be tight. Then, computing an SVD of the I/O frequency operator is sufficient for studying the I/O mode shapes. Moreover, the frequency analysis of the I/O operator highlights the resonant behavior present within the channel flow system, which indicates the presence of secondary structures that can be excited by various disturbances. Thus, structured I/O analysis is a useful tool for modal analysis that can be utilized for various types of flows such as Couette flow or flows with passive control devices such as riblets [34]. Furthermore, turbulent flows can also be studied using the I/O analysis, where the base flow is modelled as a turbulent mean flow. The extension of the structured I/O analysis to various other flows is a subject of future studies.

Acknowledgments

References

[1] Jovanović, M. R., "From bypass transition to flow control and data-driven turbulence modeling: an input–output viewpoint," *Annual Review of Fluid Mechanics*, Vol. 35, 2021.

[2] Taira, K., Brunton, S. L., Dawson, S. T. M., Rowley, C. W., Tim Colonius, B. J. M., Schmidt, O. T., Gordeyev, S., Theofilis, V., and Ukeiley, L. S., "Modal Analysis of Fluid Flows: An Overview," *AIAA Journal*, Vol. 55, No. 12, 2017.

[3] Taira, K., Hemati, M., and Ukeiley, L., "Modal analysis of fluid flows: Introduction to the virtual collection," *AIAA Journal*, Vol. 58, No. 3, 2020.

[4] Taira, K., Hemati, M., Brunton, S., Sun, Y., Duraisamy, K., Bagheri, S., Dawson, S., and Yeh, C.-A., "Modal analysis of fluid flows: Applications and outlook," *AIAA Journal*, Vol. 58, No. 3, 2020.

[5] Kerswell, R., "Nonlinear Nonmodal Stability Theory," *Annual Review of Fluid Mechanics*, Vol. 50, No. 1, 2018, pp. 319–345.

[6] Kalur, A., Seiler, P., and Hemati, M., "Stability and performance analysis of nonlinear and non-normal systems using quadratic constraints," *AIAA Aerospace Sciences Meeting, AIAA Paper 2020-0833*, 2020.

[7] Kalur, A., Seiler, P., and Hemati, M. S., "Nonlinear stability analysis of transitional flows using quadratic constraints," *Physical Review Fluids*, Vol. 6, No. 4, 2021, p. 044401.

[8] Kalur, A., Mushtaq, T., Seiler, P., and Hemati, M. S., "Estimating regions of attraction for transitional flows using quadratic constraints," *IEEE Control Systems Letters*, Vol. 6, 2021, pp. 482–487.

[9] Liu, C., and Gayme, D. F., "Input-output inspired method for permissible perturbation amplitude of transitional wall-bounded shear flows," *Phys. Rev. E*, Vol. 102, 2020, p. 063108.

[10] Liu, C., and Gayme, D. F., "Structured input–output analysis of transitional wall-bounded flows," *Journal of Fluid Mechanics*, Vol. 927, 2021.

[11] Packard, A., Fan, M., and Doyle, J., "A power method for the structured singular value," *Proceedings of the 27th IEEE Conference on Decision and Control*, 1988, pp. 2132–2137 vol.3.

[12] Zhou, K., Doyle, J., and Glover, K., *Robust and Optimal Control*, Feher/Prentice Hall Digital and, Prentice Hall, 1996.

[13] Mushtaq, T., Bhattacharjee, D., Seiler, P., and Hemati, M. S., "Structured Singular Value of a Repeated Complex Full Block Uncertainty," , 2022. https://doi.org/10.48550/ARXIV.2211.05929, URL https://arxiv.org/abs/2211.05929.

[14] Schmid, P. J., and Henningson, D. S., *Stability and transition in shear flows*, Springer, 2001.

[15] Jovanović, M. R., and Bamieh, B., "Componentwise energy amplification in channel flows," *Journal of Fluid Mechanics*, Vol. 534, 2005, pp. 145–183.

[16] Trefethen, L. N., *Spectral methods in MATLAB*, SIAM, 2000.

[17] McKernan, J., "Control of Plane Poiseuille Flow: A Theoretical and Computational Investigation," Ph.D. thesis, University of Cranfield, 2006.

[18] Packard, A., and Doyle, J., "The complex structured singular value," *Automatica*, Vol. 29, No. 1, 1993, pp. 71–109.

[19] Zhou, K., and Doyle, J. C., *Essentials of robust control*, Vol. 104, Prentice hall Upper Saddle River, NJ, 1998.

[20] Khalil, H. K., *Nonlinear systems; 3rd ed.*, Prentice-Hall, Princeton, NJ, 2002.

[21] Braatz, R. P., Young, P. M., Doyle, J. C., and Morari, M., "Computational complexity of μ calculation," *IEEE Transactions on Automatic Control*, Vol. 39, No. 5, 1994, pp. 1000–1002.

[22] Poljak, S., and Rohn, J., "Checking robust nonsingularity is NP-hard," *Mathematics of Control, Signals and Systems*, Vol. 6, No. 1, 1993, pp. 1–9.

[23] Coxson, G. E., and DeMarco, C. L., "The computational complexity of approximating the minimal perturbation scaling to achieve instability in an interval matrix," *Mathematics of Control, Signals and Systems*, Vol. 7, No. 4, 1994, pp. 279–291.

[24] Watson, G., "Computing the structured singular value," *SIAM journal on matrix analysis and applications*, Vol. 13, No. 4, 1992, pp. 1054–1066.

[25] Troeng, O., "Five-Full-Block Structured Singular Values of Real Matrices Equal Their Upper Bounds," *IEEE Control Systems Letters*, Vol. 5, No. 2, 2021, pp. 583–586.

[26] Colombino, M., and Smith, R. S., "A Convex Characterization of Robust Stability for Positive and Positively Dominated Linear Systems," *IEEE Transactions on Automatic Control*, Vol. 61, No. 7, 2016, pp. 1965–1971.

[27] Osborne, E. E., "On Pre-Conditioning of Matrices," *J. ACM*, Vol. 7, No. 4, 1960, p. 338–345.

[28] Young, P. M., Newlin, M. P., and Doyle, J. C., "Practical computation of the mixed μ problem," *1992 American Control Conference*, 1992, pp. 2190–2194.

[29] Dullerud, G. E., and Paganini, F., *A course in robust control theory: a convex approach*, Vol. 36, Springer Science & Business Media, 2013.

[30] Young, P., and Doyle, J., "Computation of mu with real and complex uncertainties," *29th IEEE Conference on Decision and Control*, 1990, pp. 1230–1235 vol.3.

[31] Reddy, S. C., Schmid, P. J., Baggett, J. S., and Henningson, D. S., "On stability of streamwise streaks and transition thresholds in plane channel flows," *Journal of Fluid Mechanics*, Vol. 365, 1998, pp. 269–303.

[32] Reddy, S. C., and Henningson, D. S., "Energy growth in viscous channel flows," *Journal of Fluid Mechanics*, Vol. 252, 1993, pp. 209–238.

[33] Thomas, L., "The stability of plane Poiseuille flow," *Physical Review*, Vol. 91, No. 4, 1953, p. 780.

[34] Chavarin, A., and Luhar, M., "Resolvent analysis for turbulent channel flow with riblets," *AIAA Journal*, Vol. 58, No. 2, 2020, pp. 589–599.